https://doi.org/10.1016/j.jmps.2020.103889

Robust 2D/3D multi-polar acoustic metamaterials with broadband double negativity

Hao-Wen Dong[1, 2†], Sheng-Dong Zhao[3,4†], Yue-Sheng Wang[5*], Li Cheng[1*], Chuanzeng Zhang[6]

[1]*Department of Mechanical Engineering, The Hong Kong Polytechnic University, Hong Kong, PR China*
[2]*Department of Applied Mechanics, University of Science and Technology Beijing, Beijing 100083, PR China*
[3]*School of Mathematics and Statistics, Qingdao University, Qingdao 266071, PR China*
[4]*Institute of Mechanics for Multifunctional Materials and Structures, Qingdao University, Qingdao 266071, PR China*
[5]*Department of Mechanics, School of Mechanical Engineering, Tianjin University, Tianjin 300350, PR China*
[6]*Department of Civil Engineering, University of Siegen, D-57068 Siegen, Germany*

Highlights

- A class of robust multi-polar multi-cavity acoustic metamaterials (AMMs) is proposed.
- Mechanisms of multi-polar resonances are accurately elucidated by equivalent LC circuits.
- Explicit relationships governing the double-negative frequency bounds are revealed.
- A simple, highly-symmetric and intuitionistic 3D AMM is proposed.
- Broadband subwavelength imaging is achieved by 2D and 3D superlens.

Abstract

Acoustic negative-index metamaterials show promise in achieving superlensing for diagnostic medical imaging. In spite of the recent progress made in this field, most acoustic metamaterials (AMMs) suffer from deficiencies such as low spatial symmetry, sophisticated labyrinth topologies and narrow-band features, which hamper their applications for symmetric subwavelength imaging. To overcome the hurdle of designing practical negative-index metamaterials, in this paper, we propose a novel category of robust multi-cavity metamaterials and reveal their common double-negative mechanism enabled by multi-polar (dipole, quadrupole and octupole) resonances in both two-dimensional (2D) and three-dimensional (3D) scenarios. In particular, we discover explicit relationships governing the double-negative frequency bounds from equivalent circuit analogy. For the first time, we construct a simple, highly-symmetric and intuitionistic 3D AMM by exploiting the multi-cavity topological features. This entails the broadband single-source and double-source subwavelength imaging, which is demonstrated and verified by 2D and 3D superlens both numerically and experimentally. Moreover, the analogical 3D superlens can ensure the subwavelength imaging in all directions. The proposed multi-polar resonance-enabled robust metamaterials and design methodology open horizons for easier manipulation of subwavelength waves and realization of practical 3D metamaterial devices.

Keywords

Acoustic metamaterial; Multi-polar resonance; Multi-cavity topology; Robust characteristics; Broadband, Double negativity; 3D Superlens

† These authors contributed equally to this work.
* Corresponding authors: li.cheng@polyu.edu.hk (L. Cheng); yswang@tju.edu.cn (Y. S. Wang)

1. Introduction

During the past two decades, choreographed artificial metamaterials (Pendry, 2000; Fang et al., 2006; Liu et al., 2000) have been explored to manipulate electromagnetic (Pendry, 2000), acoustic (Fang et al., 2006; Kaina et al., 2015; Cheng et al., 2015; Christensen et al., 2019) and elastic (Zhu et al, 2014; Dong et al., 2017; Liu et al., 2015; Sridhar et al., 2018; Sugino et al., 2018; Liu, 2019; Nathakumar et al., 2019; Morini et., 2019) wave propagations. Acoustic metamaterials (AMMs) can lead to diverse subwavelength functionalities (Ma and Sheng, 2016), such as perfect absorption (Mei et al., 2012), negative refraction (Liang and Li, 2012; Xie et al., 2013; Kaina et al., 2015; Christensen and de Abajo, 2012), asymmetric transmission (Li et al., 2017), phase modulation (Xie et al., 2014; Li et al., 2017; Xie et al., 2017; Zhu et al., 2017; Li et al., 2018;), etc., showing promise for various applications in sound reconstruction (Ma et al., 2018), imaging (Zhang et al., 2009; Zhu et al, 2011; Christensen and de Abajo, 2012; Kaina et al., 2015), energy harvesting (Qi et al., 2016), cloaking (Zigoneanu etal., 2014) and topological transmission (Xia et al., 2019), etc. Since double negativity is a cornerstone in many applications such as the super-resolution medical ultrasonic imaging, double-negative AMMs have been drawing persistent attention and also synthesized through various means such as coupled Helmholtz resonators (Zhou et al., 2018), membranes (Yang et al., 2013), combined membranes and Helmholtz resonators (Lee et al., 2010), space-coiling units (Liang and Li, 2012; Xie et al., 2013) and macroporous silicone rubber microbeads (Brunet et al., 2015). Anisotropic (Christensen and de Abajo, 2012; Shen et al., 2015) AMMs can also realize the subwavelength imaging. However, their highly unsymmetrical microstructures make them difficult to be integrated at large-scale for symmetric imaging applications.

For subwavelength airborne sound, the detuned Helmholtz resonators can be designed to create visible double negativity (Zhou et al., 2018). With the use of two coupled membranes, double negativity can also be achieved with tunable monopole and dipole resonances (Yang et al., 2013). Alternatively, combining membranes and Helmholtz resonators has been shown to enable double negativity in the ultra-low frequency range (Lee et al., 2010). Furthermore, the space-coiling structures can exhibit double negativity only in a relatively narrow frequency range (Christensen and de Abajo, 2012). As for the structural forms of double-negative solid-air microstructures, two bottle-necking problems hamper the practical 3D subwavelength imaging beyond the proof-of-concept design stage. On one hand, most previously reported space-coiling metamaterials suffer from the low spatial symmetry and sophisticated labyrinth topologies, which limit the practical applicability of double-negative AMMs for subwavelength imaging. Besides, our previous work showed that highly symmetric space-coiling metamaterials are nearly impossible to acquire double negativity (Dong et al., 2019). On the other hand, the lack of novel universal double-negative mechanism and topological feature hinders the 3D broadband subwavelength imaging.

In this article, we design, fabricate and test a novel class of multi-cavity AMMs featuring broadband double negativity. The proposed 2D multi-cavity system is demonstrated to be analogous to the inductor-capacitor circuits (LC) with intrinsic hybridization of quadrupole and dipole resonances. To validate the 2D multi-polar AMMs, we numerically and experimentally demonstrate the single-source and double-source acoustic imaging and accomplish the broadband subwavelength properties of the designed 2D superlens. As an extension, a simple, highly-symmetric and intuitionistic 3D AMM is also realized by exploiting the typical multi-cavity topological features. Then, we reveal its double-negative mechanism of intrinsic hybridization of octupole and quadrupole resonances. In particular, we discover explicit relationships governing the double-negative frequency bounds of multi-polar resonances in both 2D and 3D AMMs. The unique relationship can not only explain the observed double-negative properties but also provide simple and universal guidance for the subsequent metamaterial design. Finally, we design a 3D

superlens to realize the broadband subwavelength single-source and double-source imaging both numerically and experimentally. The most important feature about this 3D superlens is their ability of ensuring the subwavelength imaging in all directions. The proposed design concept and the revealed multi-polar resonance mechanism open new horizons for the design of 3D metamaterial devices.

2. Wave motion and effective medium description of acsoutic metamaterials

Here, we study the wave propagation within periodic arrays of the solid-air microstructures. For the wave propagation with the acoustic-elastic coupling, the harmonic wave motion inside solids is governed by

$$\nabla\left[\left[\lambda(\mathbf{r})+2\mu(\mathbf{r})\right](\nabla\cdot\mathbf{u})\right]-\nabla\times\left[\mu(\mathbf{r})\nabla\times\mathbf{u}\right]+\rho(\mathbf{r})\omega^2\mathbf{u}=0, \tag{1}$$

where λ and μ are the Lamé coefficients; $\mathbf{r}=[x\ y\ z]^{\mathrm{T}}$ represents the position vector; ρ is the mass density; ω denotes the circular frequency; $\mathbf{u}$ signifies the displacement vector; and ∇ declares the Laplace operator.

For the air host, the harmonic wave motion with behaviors of only longitudinal waves is governed by

$$\nabla\cdot\left[\rho_0^{-1}\nabla p(\mathbf{r})\right]+\omega^2\lambda^{-1}p(\mathbf{r})=0, \tag{2}$$

where ρ_0 is the mass density of air; p denotes the acoustic pressure; and λ is equivalent to the bulk modulus K_0 of air. Then $c_0=\sqrt{K_0/\rho_0}$ represents the sound velocity in air.

To solve the coupled problem in Eqs. (1) and (5), the normal displacement and force in the solid-air interface should meet the continuous conditions expressed by

$$\mathbf{u}^f\cdot\mathbf{n}=\mathbf{u}^s\cdot\mathbf{n}, \tag{3}$$

$$\boldsymbol{\sigma}\cdot\mathbf{n}=-p\mathbf{n}, \tag{4}$$

where $\mathbf{n}$ is the normal vector of the interface, pointing to the air; $\mathbf{u}^f$ and $\mathbf{u}^s$ are the displacements of fluid particles and solids, respectively; and $\boldsymbol{\sigma}$ denotes the stress tensor of the solids. In fact, the wave propagation in a solid-air system is predominant in the background air (Goffaux and Vigneron, 2001). Therefore, the acoustic governing equation in Eq. (2) is sufficient to characterize the wave motion (Goffaux and Vigneron, 2001). Using the Floquet-Bloch theory, we have $p(\mathbf{r})=e^{i\mathbf{k}\cdot\mathbf{r}}p_{\mathbf{k}}(\mathbf{r})$ and $\mathbf{u}(\mathbf{r})=e^{i\mathbf{k}\cdot\mathbf{r}}\mathbf{u}_{\mathbf{k}}(\mathbf{r})$ for the pressure and displacement, where $\mathbf{k}$ and $p_{\mathbf{k}}(\mathbf{r})$ are the Bloch wave vector of the first Brillouin zone and periodic function of $\mathbf{r}$. Solving the problem in Eqs. (1) and (2), the structural-air coupling conditions in Eqs. (3) and (4), and the periodic boundary conditions, we can derive the dispersion relation (ω–$\mathbf{k}$) using the commercial finite element software ABAQUS/Standard solver Lanczos.

To get the steady state response of the periodic solid-air medium under the incident acoustic waves, the kinematic equation is described by the finite element method in ABAQUS/Standard as

$$\begin{bmatrix}\mathbf{K}_{\mathrm{S}} & \mathbf{S}_{\mathrm{SA}}^{\mathrm{T}}\\ 0 & \mathbf{K}_{\mathrm{A}}\end{bmatrix}\begin{Bmatrix}\mathbf{u}\\ p\end{Bmatrix}-\omega^2\begin{bmatrix}\mathbf{M}_{\mathrm{S}} & 0\\ -\mathbf{S}_{\mathrm{SA}}^{\mathrm{T}} & \mathbf{M}_{\mathrm{A}}\end{bmatrix}\begin{Bmatrix}\mathbf{u}\\ p\end{Bmatrix}=\begin{Bmatrix}0\\ P_{\mathrm{A}}\end{Bmatrix}, \tag{5}$$

where $\mathbf{K}_{\mathrm{S}}$ and $\mathbf{K}_{\mathrm{A}}$ are the stiffness matrix of the solid and air parts, respectively; $\mathbf{M}_{\mathrm{S}}$ and $\mathbf{M}_{\mathrm{A}}$ are the corresponding mass matrices; $\mathbf{S}_{\mathrm{SA}}$ is the solid-air coupled matrix; and P_{A} denotes the acoustic pressure excitation.

In general, when the operating wavelength is at least 5 times larger than the lattice constant of a microstructure (Xie et al., 2013), the microstructure with exotic wave properties can be treaded as a typical metamaterial. Under the long-wavelength assumption, it is common to treat the periodic solid-air microstructures as homogenized materials characterized by effective constitutive parameters, which can be

obtained through the classic and commonly used retrieved method (Fokin et al., 2007). In this S-parameter based approach, the model under a normal incident plane wave can be regarded as a two-port network. If the homogenized microstructure has the effective mass density ρ_{eff}, bulk modulus K_{eff} and characteristic impedance Z_{eff}, the reflection (R) and transmission (T) coefficients can be extracted from

$$R = \frac{Z_{\text{eff}}^2 - Z_0^2}{Z_0^2 + Z_{\text{eff}}^2 + 2iZ_0 Z_{\text{eff}} \cot\phi_{\text{eff}}}, \tag{6}$$

$$T = \frac{Z_0(1+R)}{Z_0 \cos\phi_{\text{eff}} - iZ_{\text{eff}} \sin\phi_{\text{eff}}}, \tag{7}$$

where $Z_0=\rho_0 c_0$ expresses the characteristic impedance of the background air; $\phi_{\text{eff}}=\omega a/c_{\text{eff}}$ is the effective phase change across the homogenized microstructure; a is the lattice constant of the microstructure; and c_{eff} indicates the effective phase velocity of the microstructure.

Conversely, as long as T and R are determined by the four-microphone method (Song and Bolton, 2000), the effective refractive index n_{eff} and impedance Z_{eff} can be retrieved by

$$n_{\text{eff}} = \frac{-i\ln\xi + 2\pi m}{k_0 a}, \tag{8}$$

$$Z_{\text{eff}} = \frac{\eta}{1-2R+R^2-T^2}, \tag{9}$$

where m represents the branch number of function $\cos^{-1}[(1- R^2+T^2)/2T]$; k_0 is the wave vector of the background air; and ξ and η are given by

$$\xi = \frac{1-R^2+T^2+\eta}{2T}, \tag{10}$$

$$\eta = \mp\sqrt{(R^2-T^2-1)^2-4T^2}, \tag{11}$$

where η should be chosen to have the suitable sign so that $\text{Re}(Z_{\text{eff}})$ is physically positive. Note that only the subwavelength microstructure can guarantee the zero value of m. However, m should be finite values as integers for the thick microstructure. Anyway, the retrieved method is robust enough for the acoustic composite medium if m is correctly given.

As a result, the effective values of ρ_{eff} and K_{eff} can be obtained by

$$\rho_{\text{eff}} = \rho_0 Z_{\text{eff}} n_{\text{eff}}, \tag{12}$$

$$K_{\text{eff}} = K_0 Z_{\text{eff}} / n_{\text{eff}}. \tag{13}$$

3. Results and discussions

This section firstly presents the results and discussions for the 2D square-latticed AMMs composed of polylactice acid (PLA) and air. Subsequently, an analogical 3D cubic AMM is constructed for the broadband double negativity. The material parameters of the 2D and 3D microstructures are: the mass density ρ_{PLA}=1250 kg/m^3, ρ_0=1.29 kg/m^3, bulk modulus $K_{\text{PLA}}=3.5\times10^9$ Pa, K_0=149124 Pa, and Poission ratio υ_{PLA}=0.33. For both 2D and 3D AMMs, dispersion relations, effective constitutive parameters and eigenstates were obtained by ABAQUS 6.14-1. Simulations of subwavelength acoustic imaging through 2D

and 3D superlens were conducted by COMSOL Multiphysics 4.4. In general, for the coupled problems between two media with drastically different mechanical properties/impedances such as solid and air (also called high contrast wave problems), it is very common to treat the solids as a perfectly hard medium. But, when the microstructure possesses very complex topologies and solids with losses, considering the acoustic-structure interactions is more realistic than assuming the sound hard boundaries (Gerard et al., 2018). That is why the fully interaction model was adopted in the current study. Acoustic experiments were then conducted for demonstrating their broadband subwavelength imaging. All computations were performed on a Linux cluster with 16 cores of Intel Xeon E5-2660 at 2.20 GHz.

3.1. 2D multi-polar multi-cavity metamaterials

This section presents an inverse-designed 2D multi-cavity AMMs with broadband double negativity. The abundant numerical results about the effective constitutive parameters, typical eigenstates and the equivalent LC circuits clearly demonstrate the multi-polar double-negative properties. Meanwhile, the broadband single-source and double-source subwavelength imaging is adequately verified by simulations and experiments.

3.1.1. Design of 2D multi-cavity metamaterials

We employ topology optimization (Dong et al., 2017, 2018, 2019) to design the 2D double-negative microstructure within a target subwavelength range [0, 3000 Hz]. Since the objective function is the kernal of the topology optimization, it is necessary to construct an objective function including the negative mechanisms and special structural constraints to obtain the ideal double-negative metamaterials (Dong et al., 2019). To be specific, both ρ_{eff} and K_{eff} should increase simultaneously within the frequency range to capture the novel topological features different from the existing space-coiling metamaterials. The value of n_{eff} should be large enough to induce the desired resonances. At the same time, the microstructure must contain just only one air region for ensuring the reasonable topology and wave propagation path. To meet the manufacturing requirement, we have to introduce constraints for ensuring the processable solid and air components (Dong et al., 2019). Details of the optimization formulation are given in Appendix A.

To facilitate the optimization, we assume that the primitive microstructure has a square symmetry. An arbitrary microstructure is divided into 60×60 pixels and treated as a binary chromosome. In the initial stage of GA, a population consisting of 30 chromosomes is randomly generated. Then, an "abuttal entropy filter" method (Dong et al., 2017, 2018, 2019) is applied to improve the topological forms of chromosomes. After determining the fitness of every involved chromosomes, the algorithm adopts the tournament selection strategy with the size of competition group N_{ts}=18 to execute the reproduction. To be specific, 18 randomly selected chromosomes will compete to each other based on their fitness values. Then, the best chromosome will be put into the mating pool. After 30 times of competitions, the mating pool will contain 30 selected excellent chromosomes for the next round of genetic operation. Then, the crossover operation with the crossover probability P_{c}=0.9 and mutation operation with the mutate probability P_{m}=0.02 are carried out to generate the offspring population. In addition, the elitism strategy is used to accelerate the evolution process. When the evolution reaches a given iteration number (5000), GA produces an optimized solid-air microstructure with broadband double negativity within the prescribed frequency range.

Using the above inverse-design methodology, we design and fabricate a 2D microstructure comprising five big solid blocks, four narrow air channels and four air regions, as shown in Figs. 1(a) and 1(b). The retrieved normalized effective mass density ρ_{eff}/ρ_0 and the bulk modulus K_{eff}/K_0 in Figs. 1(c) and 1(d)

confirm the double negativity within [1682.7 Hz, 2419.5 Hz]. Up to now, for the solid-air metamaterials, only the work on space-coiling metamaterials claimed the broadband double negativity within [2100 Hz, 2600 Hz] (Xie et al., 2013), corresponding to a relative bandwidth of about 21.3%. The relative bandwidths reported by other works on solid-air acoustic metamaterials typically range from 8.4% (Zhou et al., 2018) to 16.7% (Liang and Li, 2012). Therefore, compared with the existing results, the designed double-negative AMM with the relative bandwidth of 35.9% in Fig. 1 can be regarded as a broadband metamaterial.

Notably, the broadband negative range of ρ_{eff} is much larger than that of K_{eff}; and consequently, the latter dominates the resulting double-negative range. Importantly, compared with the space-coiling AMMs (Liang and Li, 2012; Xie et al., 2013; Cheng et al., 2015), the multi-cavity AMMs in Fig. 1 essentially reduce the structural requirements for double-negative formation. To quantify the effect of viscous loess on double negativity, we adopt the simplified model of $k_0 = \omega/c_0 - \gamma_{\text{loss}} \times i\,\omega/c_0$ (Cheng et al., 2015), where γ_{loss} denotes the loss factor. Figures 1(c) and 1(d) also show that the double negativity can be effectively maintained even when the viscous losses (Cheng et al., 2015) are considered. Despite the obvious shift of the resonant frequencies, the double-negative range can be significantly extended. Since the loss can affect the transmission and the resonant frequency (Ward et al., 2015), the large loss can make the resonance around 2.5 kHz disappear in the present case. Therefore, compared with the low-loss cases (loss=0, 0.1), K_{eff} shows a significantly different tendency when the loss factor is very large (loss=0.5). Of course, with a narrower air channel, the double negativity can be further improved on the premise of an acceptable transmission. Figure 1(e) depicts the amplitude and the phase of transmission for one microstructure. It is clear that the transmission reaches the extremum at the resonant frequency and decreases visibly when frequency further increases.

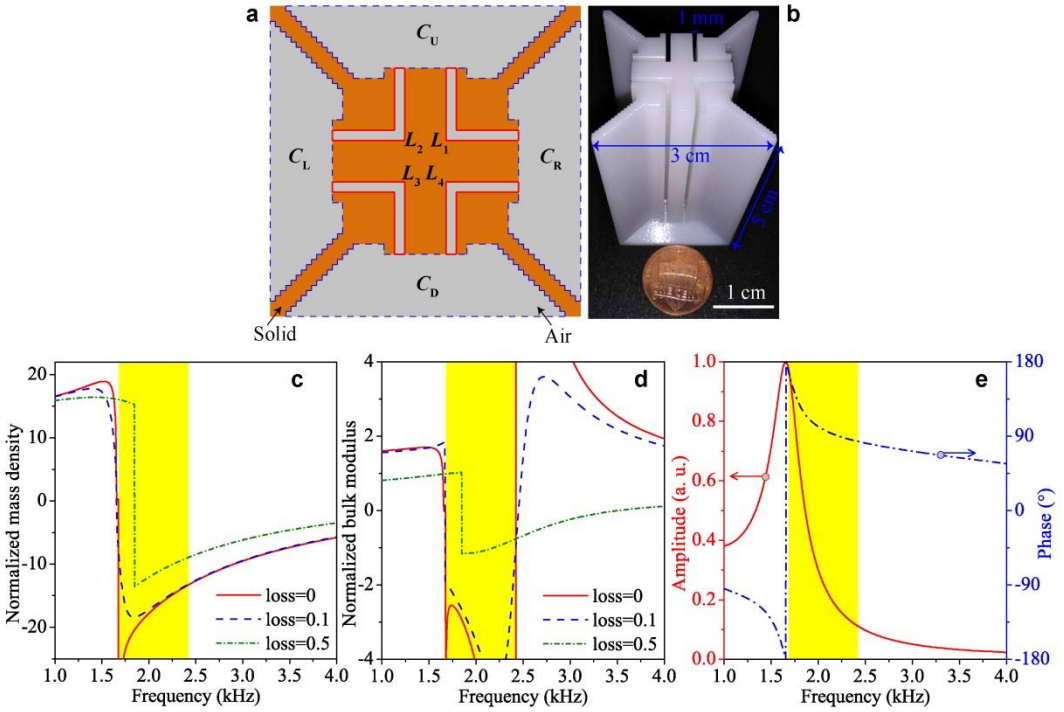

FIG. 1. 2D multi-cavity AMMs. (a) A topology-optimized solid-air microstructure. **(b)** A fabricated sample. **(c)-(d)** Effective parameters with different viscous losses. **(e)** Amplitude and phase of transmission coefficients for one microstructure without loss. The shaded regions indicate the negative-index range irrespective of viscous loss (loss=0).

3.1.2. Multi-polar mechanisms of 2D multi-cavity metamaterials

To understand the underlying physics of the observed double negativity, we scrutinize in Figs. 2(a)-2(c) three special eigenstates of AMMs in Fig. 1. Figure 2(a) clearly shows a typical quadrupole resonance behavior. The acceleration distribution is similar with the velocity distribution at **k**=0. The symmetric and diametrical distribution along *x*- and *y*- axes implies that the average velocity (v) over the microstructure is equal to zero, *i.e.* no air flowing through the structure. Besides, the amount of air flowing into or out of the microstructure can be equivalent to $\partial V/\partial t$, *i.e.* $a\cdot v=\partial V/\partial t$, where V and a are the volume and lattice constant of the microstructure, respectively. Therefore, ∂V should be zero as well. In view of the basic definition $K_{\text{eff}}=-V\partial p/\partial V$, the resultant effective modulus should be infinite. Hence, the highly symmetric cavities can provide ideal structural building blocks for negative K_{eff}. From the opposite distributions in Figs. 2(b) and 2(c), it is recognized that the average particle acceleration ($\partial v/\partial t$) over the microstructure is negative, alongside a negative divergence of the pressure. Negative ρ_{eff} can then be deduced from Newton's equation $-\nabla p=\rho_{\text{eff}}\partial v/\partial t$. Therefore, the eudipleural topological feature of the microstructure ensures the occurrence for a negative ρ_{eff}.

In view of the conspicuous resonant traits in Figs. 2(a) and 2(b), we can adopt the equivalent LC circuit (Fang et al., 2006) shown in Figs. 2(d) and 2(e) to analyze the resonant frequencies of the quadrupole and dipole resonances, respectively. To enable the analogy, the air domain in Fig. 1(a) is divided into four cavities (C_{L}, C_{R}, C_{D}, C_{U}) and four air channels (L_1, L_2, L_3, L_4). For the eigenstate in Fig. 2(a), the acoustic pressure fields in the four cavities and channels form a typical quadrupole resonance. Based on the acousto-electrical analogy, the four air cavities and channels are equivalent to the four capacitors ($C_{\text{L}}=C_{\text{R}}=C_{\text{D}}=C_{\text{U}}=C_{2\text{eff}}$) and four inductors ($L_1=L_2=L_3=L_4=L_{2\text{eff}}$) in Fig. 2(d). For the dipole resonance in Figs. 2(b) and 2(c), the acoustic pressure is mainly accentuated in the left and right air cavities and four channels. So the equivalent circuit can be simplified as two capacitors and four inductors as illustrated in Fig. 2(e). As a result, the resonant frequencies of the quadrupole ($f_{2\text{Q}}$) and dipole ($f_{2\text{D}}$) resonances can be estimated by

$$f_{2\text{Q}}=\frac{1}{2\pi\sqrt{L_{2\text{eff}}C_{2\text{eff}}/4}}, \tag{14}$$

and

$$f_{2\text{D}}=\frac{1}{2\pi\sqrt{L_{2\text{eff}}C_{2\text{eff}}/2}}, \tag{15}$$

where $C_{2\text{eff}}=V_{\text{C}}a^2/K_0$ with V_{C} being the volume fraction of one cavity; and $L_{2\text{eff}}$ is calculated by $L_{2\text{eff}}=\rho_0 l_{\text{L}}/(w_{\text{L}})$ in which l_{L} and w_{L} denote the effective length and cross-sectional width of one channel normalized to the lattice constant, respectively. The predicted relative double-negative bandwidth is 34.3% which is very close to 35.9% extracted from Figs. 1(c) and 1(d).

Intriguingly, the two resonant frequencies are directly linked to each other through a constant of $\sqrt{2}$. This specific property is attributed to the typical feature of the multi-cavity AMMs with multi-polar resonances. We can then surmise that all symmetric multi-cavity metamaterials should have a broadband double negativity within the ascertainable frequency bounds. Figures 2(f) and 2(g) depict the variations of the quadrupole resonance frequency with three predominant parameters, V_{C}, w_{L} and l_{L}. Clearly, narrow and long air channels combined with large cavities are beneficial to the low-frequency double negativity. When l_{L} keeps in constant, w_{L} can cause a greater impact on $f_{2\text{Q}}$ than V_{C}, see Fig. 2(f). However, both V_{C} and l_{L} can

have conspicuous effect on f_{2Q} when w_L is given, see Fig. 2(g). Consequently, one can easily adjust these three decisive parameters to tune the double-negative property, thus avoiding the complex topology and multiple parameters involved in the space-coiling metamaterials (Liang and Li, 2012; Xie et al., 2013).

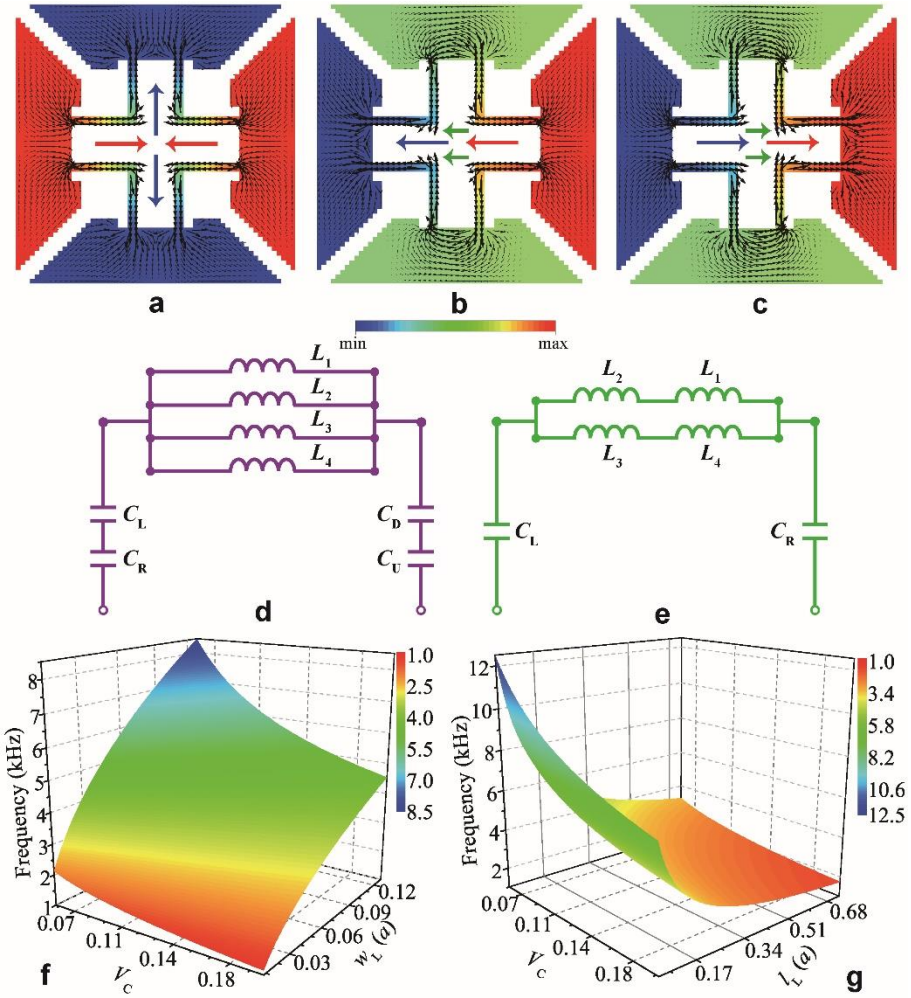

FIG. 2. 2D double-negative mechanisms. (a) Eigenstate with acceleration distribution at 2419.5 Hz and **k**=(0, 0). **(b)-(c)** Eigenstates with acceleration (b) and velocity (c) distributions at 1682.7 Hz and **k**=(π/a, 0). **(d)-(e)** Equivalent LC circuits for the eigenstates in (a) and (b). **(f)-(g)** Predicted quadrupole resonance frequencies by the circuit in (d) with three decisive parameters V_C, w_L and l_L. Values of l_L in (f) and w_L in (g) are 0.43a and 0.033a, respectively.

3.1.3. Demonstrations of broadband subwavelength imaging of 2D metamaterials

To show the potential of the proposed multi-cavity topologies, we demonstrate the broadband single-source and double-source subwavelength imaging by the designed 2D AMM. Figures 3(a) and 3(b) depict the experimental setup with a metalens where the nearly closed air cavities distribute symmetrically around the solid cross blocks.

We first investigate the single-source imaging. Figure 3(c) illustrates the acoustic pressure field due to an acoustic point source. The acosutic imaging is generated by the metamaterial slab. Undoubtedly, the imaging is ascribed to the double negativity. Figure 3(d) shows the measured normalized intensity profiles in which the single peak is consistent with the simulated results in Fig. 3(c). Both the simulated and experimentally measured half maximum (FWHM) of images in Fig. 3(e) show a breaking-down of the diffraction limit of 0.5λ at 1950 Hz, demonstrating the subwavelength imaging ability. Figure 3(f) clearly shows the broadband feature of measured imaging. Notably, one can tactically adjust the geometrical sizes of

the AMM to achieve a broader and lower frequency range. Moreover, most full widths at the half maximum (FWHM) of measured images as displayed in Fig. 3(g) can break the diffraction limit of $0.5\lambda_0$ (λ_0 refers to the acoustic wavelength in air) within the measured frequency range, thus manifesting the broadband subwavelength nature.

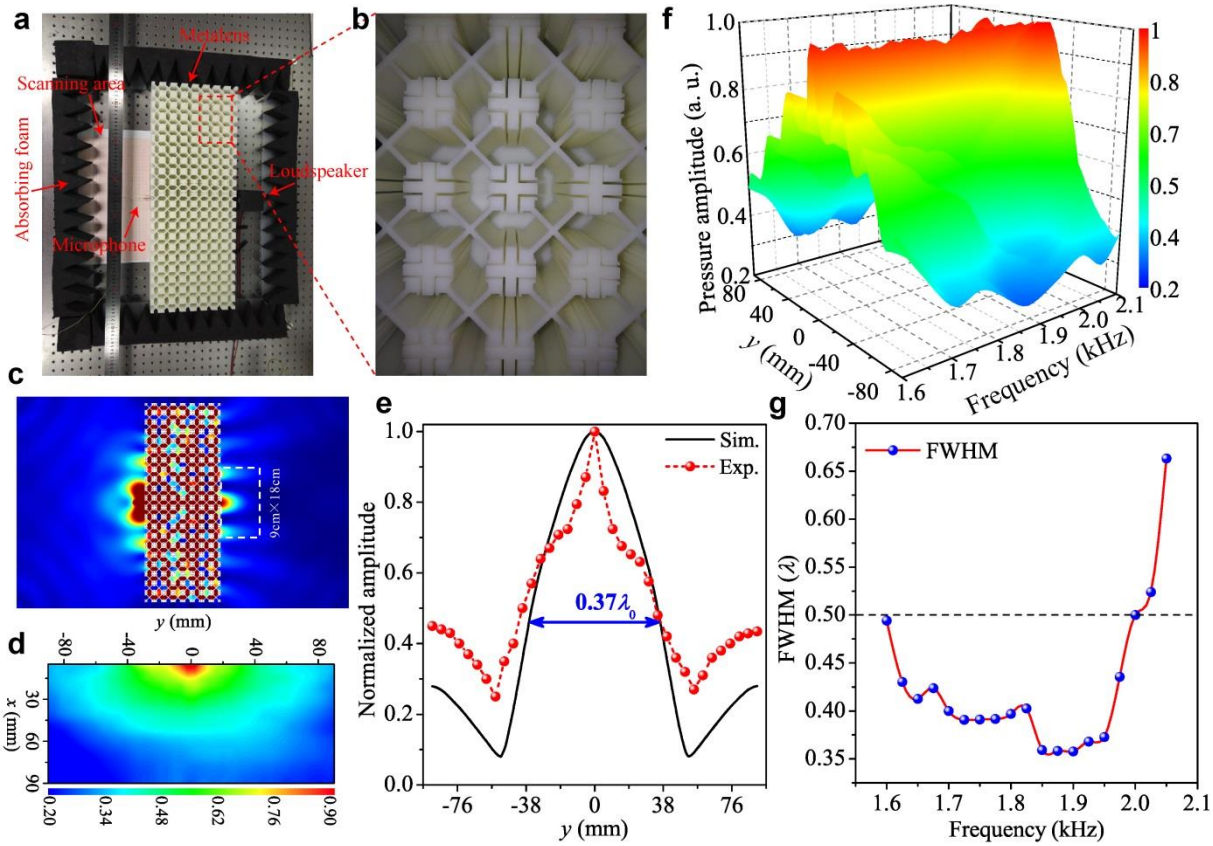

FIG. 3. Subwavelength single-source imaging by 2D AMMs. (a) Experimental setup. **(b)** Local image of the superlens comprising 21×8 microstructures. **(c)** Simulated single-source imaging at 1950 Hz. The acoustic source is located 3 cm away from the left side of the superlens containing 21×8 microstructures. **(d)** Measured acoustic amplitude field inside a scanning domain of 9 cm×18 cm shown in (c). **(e)** Simulated and measured normalized intensity profiles of the imaging in (c) and (d). **(f)** Normalized measured pressure amplitude along the exiting surface of the metamaterial slab within [1600 Hz, 2100 Hz]. For every measured frequency, the pressure amplitude profile shows the normalized amplitude to the corresponding maximal value. **(g)** Measured single-source imaging resolutions within the double-negative range.

Similarly, 2D multi-polar AMMs can also allow a double-source subwavelength imaging as shown in Fig. 4(a). The measured acoustic field in Fig. 4(b) basically matches with the simulated results in Fig. 4(a). However, two asymmetric images may be caused by the manufacturing and processing errors in the experiments. Two images are effectively separated in Fig. 4(c), thereby forming a subwavelength imaging resolution of $0.34\lambda_0$. To validate the stable imaging ability, we also check the imaging performance by varying the phase difference between the two sources. As depicted in Fig. 4(d), it can be seen that two ideal images can always be obtained within a phase shift of π. Of course, from Figs. 4(d) and 4(e), the covered range will become significantly wider if the distance between the two sources is larger. Figure 4(e) suggests that two well-separated images can be captured irrespective of the superposition produced by the phase shift from 50° to 310°. The measured profiles and maps also demonstrate the stable subwavelength imaging resolutions. In short, two images can be effectively distinguished over the large phase-shift range. All measured imaging results also demonstrate that the viscous losses can hardly affect the double-negative

properties, in agreement with the results in Figs. 1(c) and 1(d).

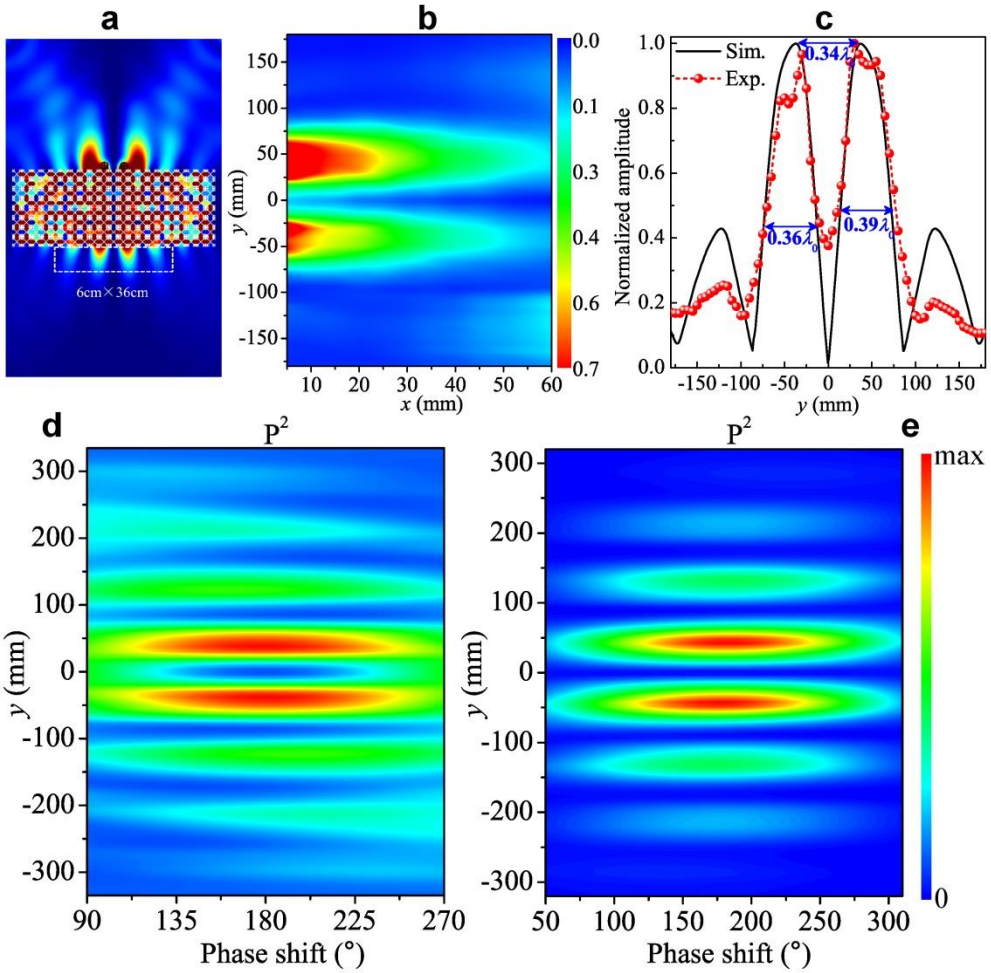

FIG. 4. Subwavelength double-source imaging by 2D AMMs. (a) Simulation for two point sources (6 cm apart) with a phase shift of π at 1950 Hz. Dashed region represents the measured domain of 6 cm×36 cm. **(b)** Measured acoustic amplitude field within a scanning domain shown in (a) at 1950 Hz. **(c)** Simulated and measured sound intensity profiles of imaging under two-point sources (6 cm apart) with a π phase shift at 1950 Hz. **(d)-(e)** Simulated maps of the intensity distribution in the focal plane with a phase shift between the two point sources at 1950 Hz under distances of 6 cm (c) and 9 cm (d).

3.2. 3D multi-polar multi-cavity metamaterials

Inspired by the multi-cavity topology of the above designed 2D AMM, we propose an analogical 3D multi-cavity AMMs with broadband double negativity in this section. Numerical results about the band structures, effective constitutive parameters, typical eigenstates and the equivalent LC circuits clearly demonstrate the high-order multi-polar double-negative properties. The broadband single-source and double-source subwavelength imaging is realized by a very simple 3D superlens. The corresponding imaging ability is verified through simulations and experiments as well.

3.2.1. Analogical 3D multi-cavity metamaterials

Since the 2D multi-cavity topologies with multi-polar resonances are the intrinsic topological features, as long as we can capture these features, it should be straightforward to construct the analogical 3D double-negative AMMs with the simple, highly-symmetric and intuitionistic geometries. We can then

demonstrate the broadband single-source and double-source subwavelength imaging as well. The analogical 3D AMM is composed of twelve symmetric air cavities, twenty-four air channels and one solid block, see Figs. 5(a)-5(c). Each facet of the 3D microstructure has a similar topological feature as the 2D model in Fig. 1. As demonstrated below, the proposed multi-polar resonance-enabled topologies really can ensure the double negativity. Therefore, the multi-polar mechanism and multi-cavity topology are robust for double-negative solid-air AMMs.

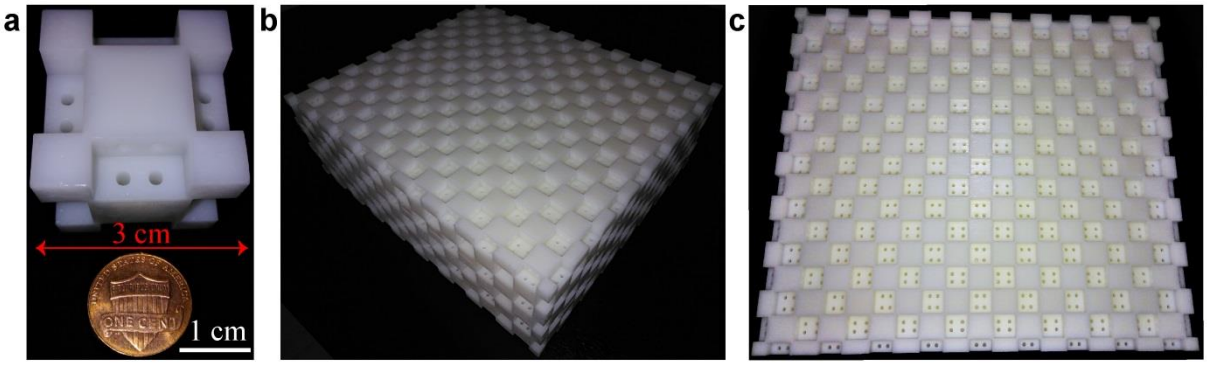

FIG. 5. 3D multi-cavity AMMs. (a) A fabricated 3D solid-air microstructure. **(b)** Photograph of a 3D superlens containing 8×9×3 microstructures. **(c)** Top view of the 3D superlens.

3.2.2. Multi-polar mechanisms of 3D multi-cavity metamaterials

From the band structure in Fig. 6(a), it is observed that the second band becomes a negative band which clearly shows the broadband negativity within [2436.5 Hz, 3083.4 Hz]. Similar isotropic behavior can be seen from nearly the same curvatures of the negative bands along the ΓX(ΓY) and ΓM directions. In particular, unlike the 2D case, there exists an anisotropic band (the third band) within the same frequency range. Clearly, the negative group velocity can be realized when the wave propagates along the ΓM direction. However, nearly zero group velocity appears when the wave propagates along the ΓX(ΓY) direction. The corresponding anisotropic wave motion should be caused by the coupling among the resonances in different planes. It is relevant to note that this coupling effect is pervasive in the 3D sonic crystals. Fortunately, at least for the present case, the following simulated and measured results fully prove that the imaging effect which originated from the double negativity is completely unaffected by the resonance coupling. As shown in Fig. 6(b), the properties of ρ_{eff} and K_{eff} clearly reveal a double-negative range that precisely matches the negative band range in Fig. 6(a). Meanwhile, the negative n_{eff} and positive Z_{eff} occur in the same range as well, see Fig. 6(c). The single negative properties in Figs. 6(b) can accurately predict a complete bandgap above the negative band. This property can also be proved by the zero n_{eff} and Z_{eff} in Fig. 6(c). Figure 6(d) illustrates the amplitude and the phase of transmission for one 3D microstructure. Obviously, the transmission reaches the extremum at the resonant frequency and decreases visibly with the increasing frequency.

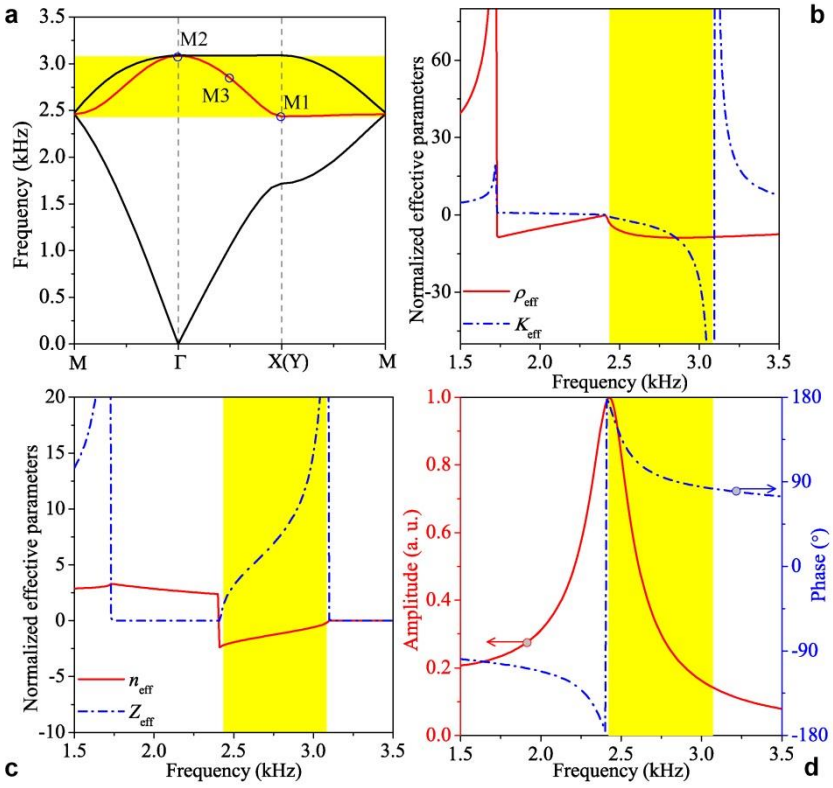

FIG. 6. Characterizations of 3D multi-cavity AMMs. (a) Dispersion relations of the microstructure in Fig. 5. **(b)-(c)** Performances of the effective constitutive parameters along the ΓX (ΓY) direction. **(d)** Amplitude and phase of transmission coefficients for one microstructure without loss. The shaded regions indicate the negative-index range.

For explaining the double negativity, Figs. 7(a) and 7(b) show the octupole and quadrupole resonances, respectively. Due to the highly symmetrical distribution of sound pressure in Figs. 7(a), it is noted that the average velocity over the microstructure is equal to zero, leading to an infinite K_{eff}. However, in view of the symmetrical pressure distribution in Fig. 7(b), zero acceleration can be generated for the entire structure. Therefore, the resultant ρ_{eff} should be infinite. Consequently, the hybridization of the quadrupole and octupole resonances induces a 3D double negativity. Indeed, the eigenstate in Fig. 7(c) shows the hybrid pressure distribution through the overlapping effect of the octupole and quadrupole resonances. To more clearly explore the double-negative essence, we evidently shows in Fig. 7(d) the octupole resonance with zero average velocity over the microstructure. The eigenstate in Fig. 7(e) indicates the quadrupole resonance with zero accelerations for the whole structure. These properties form the origin of the double negativity for 3D microstructures.

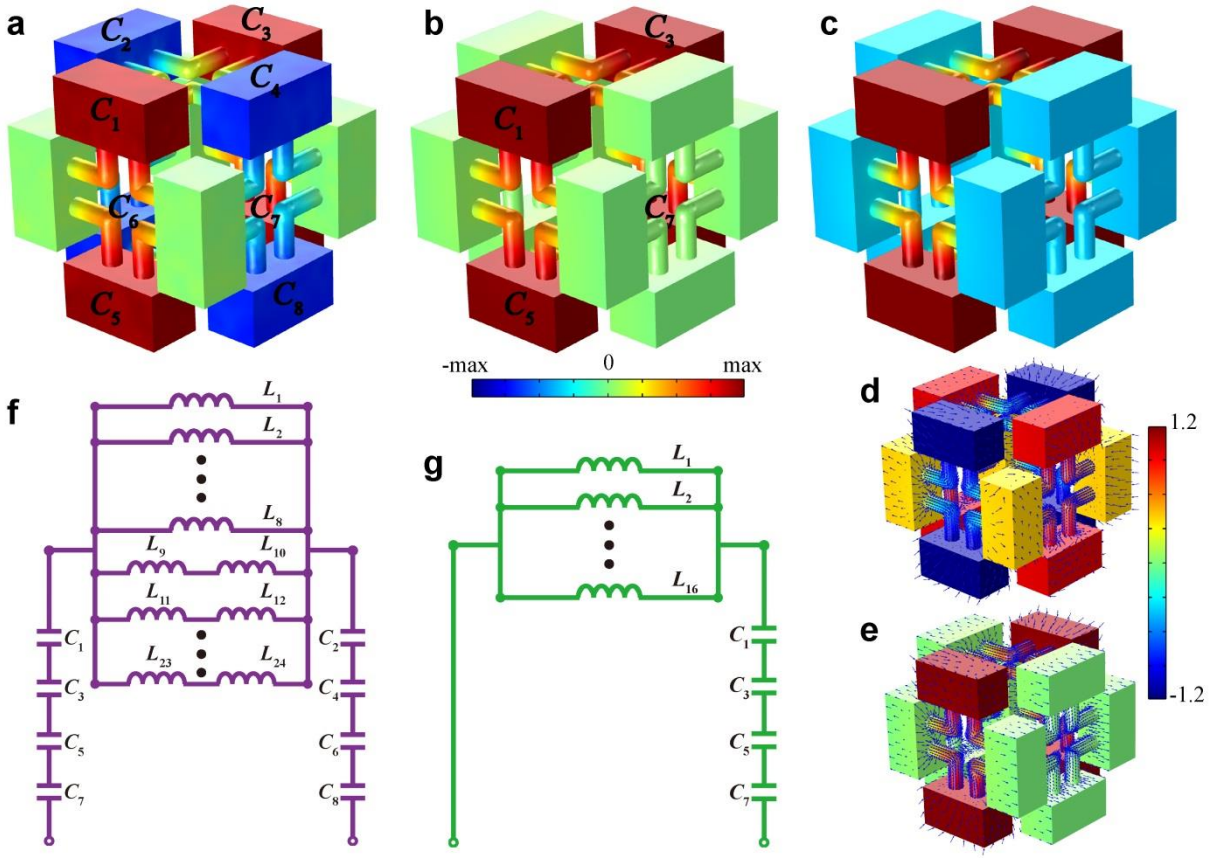

FIG. 7. 3D double-negative mechanisms. (a)-(c) Representative eigenstates M2 (a) with **k**=(0, 0, 0) at 3083.4 Hz, M1 (b) with **k**=(0, π/a, 0) at 2436.5 Hz and M3 (c) with **k**=(0, 0.5π/a, 0) at 2848.7 Hz. **(d)** The eigenstate near **k**=(0, 0, 0) with the velocity distribution. **(e)** The eigenstate M1 with the acceleration distribution. **(f)-(g)** Equivalent LC circuits of eigenstates M2 (a) and M1 (b).

Similarly, we can use an equivalent LC circuit to characterize the resonant behavior. For the octupole resonance, as shown in Fig. 7(f), eight air cavities and twenty-four tunnels dominate the acoustic pressure filed and form the typical octupole resonance. So the cavities and tunnels are equivalent to the eight capacitors (C_1=C_2…=C_8=$C_{3\text{eff}}$) and twenty-four inductors (L_1=L_2…=L_{24}=$L_{3\text{eff}}$), respectively. For the quadrupole resonance, as displayed in Fig. 7(g), only four cavities and sixteen tunnels are heavily loaded by the acoustic pressure. So the equivalent circuit has only four capacitors and sixteen inductors. As a result, the resonant frequency of the 3D octupole ($f_{3\text{O}}$) and quadrupole ($f_{3\text{Q}}$) resonances can be predicted, respectively, by

$$f_{3\text{O}} = \frac{1}{2\pi\sqrt{L_{3\text{eff}} C_{3\text{eff}}/6}}, \tag{16}$$

and

$$f_{3\text{Q}} = \frac{1}{2\pi\sqrt{L_{3\text{eff}} C_{3\text{eff}}/4}}, \tag{17}$$

where $C_{3\text{eff}}$ and $L_{3\text{eff}}$ are homoplastically defined as $C_{3\text{eff}} = V_{\text{C}} a^3/K_0$ and $L_{3\text{eff}} = \rho_0 l_{\text{L}}/(\pi r_{\text{L}}^2)$, respectively, with V_{C} being the volume fraction of one cavity; and l_{L} and r_{L} are the effective length and radius of one tunnel, respectively. The relative double-negative bandwidth is predicted to be 20.2%, fairly close to 23.4% extracted from the dispersion relations. In particular, a fixed relationship of $\sqrt{1.5}$ between $f_{3\text{O}}$ and $f_{3\text{Q}}$ is

observed. This emphasizes again the unique rule of the multi-polar resonance-enabled multi-cavity topologies even for 3D metamaterials. If other types of multi-cavity topologies are used, a fixed homologous relationship is also expected. According to Eqs. (24) and (25), three decisive parameters V_C, r_L and l_L dominate the double-negative range. Similarly, the larger cavities connected with the narrower and longer channels are favorable to double negativity at the lower frequencies.

Figures. 8(a) and 8(b) show the predicted octupole resonance frequency f_{3O} with the variations of the three decisive parameters V_C, r_L and l_L. Clearly, narrow and long air channels combined with large cavities are beneficial to the low-frequency double negativity. When l_L is kept constant, r_L exerts greater impact on f_{3O} than V_C does. However, both V_C and l_L can have conspicuous effect on f_{3O} if r_L is kept constant. Accordingly, one can easily adjust these three decisive parameters to tune the double-negative property within any desired frequency range. Compared with the 2D system in Figs. 2(f) and 2(g), the predicted frequency of the 3D case in Fig. 8 can be modulated to a much lower extent. Obviously, the predicted 2D and 3D resonance frequencies show the same dependence on three decisive structural parameters. For both 2D and 3D systems, the proposed multi-polar resonance-enabled multi-cavity topology is robust and suitable for constructing arbitrary broadband double-negative solid-air AMMs.

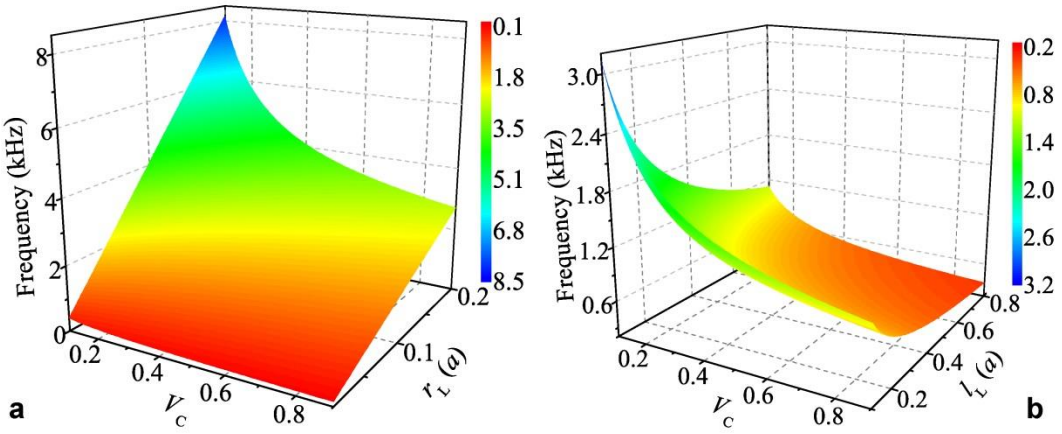

FIG. 8. Predicted octupole resonance frequencies of 3D AMMs. (a)-(b) Freuencies calculating from the equivalent LC circuit in Fig. 7 with various combinations of decisive parameters V_C, r_L and l_L. Values of l_L in (a) and r_L in (b) are $0.37a$ and $0.04a$.

3.3. Demonstrations of broadband subwavelength imaging of 3D metamaterials

The subwavelength single-source and double-source imaging can also be realized by the proposed 3D AMM, which is verified both numerically and experimentally. For the 3D imaging, the 3D acoustic experiments were conducted in a semi-anechoic room, as shown in Fig. 9(a). A loudspeaker was taken as a single point source and located a certain distance from the input interface of the metalens, while the mounted microphone recorded the acoustic pressure over the entire scanning area. For the double-source experiments, two loudspeakers with a given phase delay and distance were used asdouble point sources. Signals obtained at each position in the scanning area were averaged over four measurements. The whole acoustic filed was obtained by using the Fourier transform after the scanning measurement.

Figures 9(b) and 9(c) clearly show the simulated and measured ideal imaging at 2650 Hz. In particular, the thickness of the three layers is already sufficient for the imaging. This idiosyncrasy greatly improves the effectiveness of the multi-cavity topologies. Figure 9(d) displays the simulated and measured intensity profiles for the focal plane at 2650 Hz. The obvious peak shows a subwavelength imaging resolution of $0.42\lambda_0$. Moreover, the ideal broadband imaging can be observed from Fig. 9(e). As shown in Fig. 9(f), the measured resolutions within the frequency range of [2450 Hz, 2850 Hz] effectively demonstrate the

broadband subwavelength imaging ability in Fig. 9(e). Because of the high symmetry, the 3D AMM can safeguard the realization of imaging for acoustic waves perpendicularly incident on every facet of the sample. Certainly, the higher symmetric 3D AMM is easy to be constructed as long as the multi-polar resonance-enabled topological features are captured. Furthermore, it is intended to perform 3D topology optimization and generate some deeply practical resonance mechanism based on the multi-polar 3D AMMs in the future. These advantages will lay the foundation of deep-subwavelength ultrasound imaging.

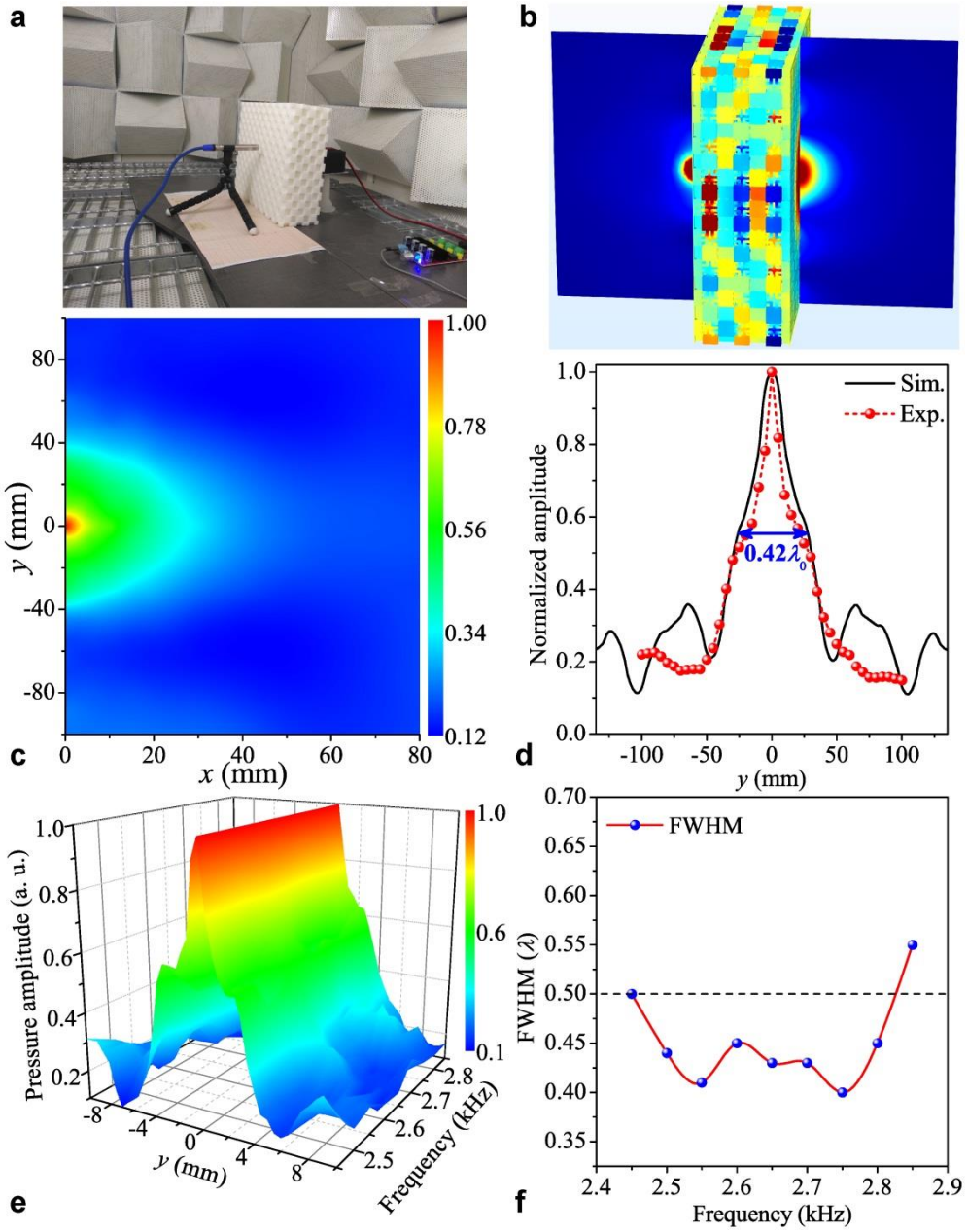

FIG. 9. Subwavelength single-source imaging by 3D AMMs. (a) 3D experimental setup. **(b)** Simulated single-source imaging at 2650 Hz. The acoustic source is located 3 cm away from the left side of the superlens. **(c)** Measured acoustic amplitude field at 2650 Hz. **(d)** Simulated and measured normalized intensity profiles of the imaging in (b). **(e)** Normalized measured acoustic pressure amplitude field along the exiting surface for a single source within [2450 Hz, 2850 Hz]. For every measured frequency, the pressure amplitude profile shows the normalized amplitude to the corresponding maximal value. **(f)** Measured single-source imaging resolutions within the operating frequency range.

In addition, Figure 10(a) clearly shows the acoustic imaging for two point sources with a phase shift of

π. The measured imaging filed in Fig. 10(b) is highly coincident with the simulated result in Fig. 10(a). Meanwhile, the simulated and measured intensity profiles in Fig. 10(c) show a subwavelength imaging resolution of $0.46\lambda_0$. Moreover, whatever the phase shift is, two well separated foci can be obtained effectively as shown in Fig. 10(d). This testifies the robustness of the double negativity and the stability of the 3D AMMs for the broadband subwavelength imaging.

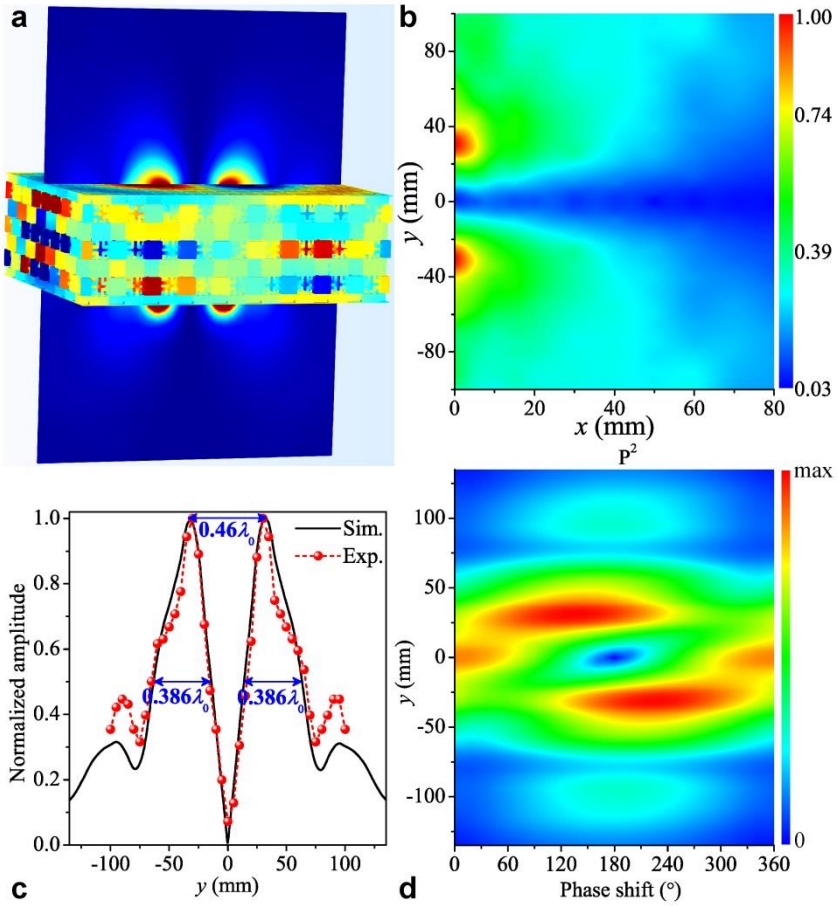

FIG.10. Subwavelength double-source imaging by 3D AMMs. (a) Simulated double-source imaging at 2650 Hz for two point sources (6 cm apart) with a π phase shift at 2650 Hz. **(b)** Measured acoustic pressure amplitude field at 2650 Hz. **(c)** Simulated and measured normalized intensity profiles for the imaging in (a). **(d)** Simulated map of the intensity distribution in the focal plane with the phase shift between the two sources from 0° to 360°.

4. Conclusions

In conclusion, we propose a new kind of multi-polar resonance-enabled robust topologies to construct both 2D and 3D broadband double-negative AMMs. Benefiting from the high symmetries, the 2D AMMs can support the combination of quadrupole and dipole resonances. Similarly, the extension of the proposed topologies to 3D enables the hybridization of octupole and quadrupole resonances. For either 2D or 3D AMMs, an explicit relationship governing the double-negative frequency bounds of multi-polar resonances is revealed. This discovery can be used as a universal criterion for double-negative multi-cavity metamaterial design. Finally, we demonstrate the broadband single-source and double-source subwavelength imaging of 2D and 3D superlens. The relatively simple, highly-symmetric, intuitionistic and robust multi-cavity topologies based on the unified multi-polar resonance mechanism are expected to boost the practical realization of the broadband superlens. The proposed design and methodology offer possibilities for airborne sound modulation using high practical 3D metamaterials (Kadic et al., 2019). In particular, we reveal a novel

multi-polar double-negative mechanism and establish equivalent LC models, which provides a sensible explanation on the observed physical phenomena and may also serve to guide the initial design. Based on the proposed LC models, it is possible to design the key parameters for the desired frequency range. Subsequently, we can construct any practical double-negative 2D/3D metamaterials according to the performance/parameters to be achieved.

It should be stressed that the proposed AMMs cannot realize the double negativity and high transimission within the entire broadband frequency range simuatensouly. Future work is needed to perform topology optimization of 3D double-negative AMMs to further increase the performance of the design in order to cope with the required high efficiency. Moreover, compared with the passive ways, the promising active approaches (Chen et al., 2018; Li et al., 2018) are expected to enable our proposed metamaterials to support the wider double-negative bandwidth and intelligently control the desired wave motions.

Acknowledgements

This work is supported by the Hong Kong Scholars Program (No. XJ2018041), the National Natural Science Foundation of China (Grant Nos. 11802012, 11532001 and 11902171), the Postdoctoral Science Foundation (2017M620607), the Fundamental Research Funds for the Central Universities (Grant No. FRF-TP-17-070A1), the Sino-German Joint Research Program (Grant No. 1355) and the German Research Foundation (DFG, Project No. ZH 15/27-1). We would like to thank Prof. Bilong Liu (Qingdao University of Technology, PR China) for his helpful participation.

Appendix A. Topology optimization formulation

To obtain the sufficiently broadband double negativity within the prescribed frequency range [0, 3000 Hz], the optimization herein with several geometrical constraints is mathematically defined as

$$Maximize: C(\Sigma)=N_{\mathrm{D}}(\Sigma)+\frac{n_0\times n_0}{11}-\frac{1}{11}\times\max\left\{\frac{\max\limits_{\nabla m\subset(1,2,\cdots 11)}\left[\rho_{eff}^{+}(m)\right]}{\min\limits_{\nabla m\subset(1,2,\cdots 11)}\left[\rho_{eff}^{+}(m)\right]},\frac{\max\limits_{\nabla n\subset(1,2,\cdots 11)}\left[K_{eff}^{+}(n)\right]}{\min\limits_{\nabla n\subset(1,2,\cdots 11)}\left[K_{eff}^{+}(n)\right]}\right\}, \tag{A1}$$

$$Subject\ to: U_{\mathrm{A}}=1, \tag{A2}$$

$$\min_{\Sigma}(w_{\mathrm{A}},w_{\mathrm{S}})\geq a/30, \tag{A3}$$

$$\min_{\substack{m=1,2,\cdots 11\\ n=1,2,\cdots 11}}\left\{\left[\rho_{eff}^{+}(2)-\rho_{eff}^{+}(1),\cdots\rho_{eff}^{+}(m)-\rho_{eff}^{+}(m-1)\right],\left[K_{eff}^{+}(2)-K_{eff}^{+}(1),\cdots K_{eff}^{+}(n)-K_{eff}^{+}(n-1)\right]\right\}>0, \tag{A4}$$

where the targeted frequency range is represented by 11 uniformly distributed discrete frequencies. All physical quantities are tabulated in Table A1. In particular, the constraint (A4) can guarantee the simutaneous increasing mechanism (Dong et al., 2019). If the air channel gets narrower, a larger double-negative bandwidth should appear in the lower frequency range. However, the limitation in the manufacturing capability prevents the size of the air channel from being be infinitesimal. Therefore, the optimal value in the optimization framework is $a/30$ as shown in Eq. (A3). With increasing N_{D} during the evolution, microstructure volutes with a wider double-negative range.

Physical quantity	Definition
Σ	Topological distribution within the microstructure
C	Objective function describing the double-negative bandwidth
N_D	Number of the discrete frequencies with simutaneous negative ρ_{eff} and K_{eff}
n_0	Quasi-static effective index of the microstructure
ρ_{eff}^{+}	Set consisting of serveral values of the positive ρ_{eff} at some discrete frequencies
K_{eff}^{+}	Set consisting of serveral values of the positive K_{eff} at some discrete frequencies
m	Serial number of the discrete frequency with the positive ρ_{eff}
n	Serial number of the discrete frequency with the positive K_{eff}
U_A	Number of the continuous air domains within the microstructure
w_A	Set consisting of widths of all air connections within the microstructure
w_S	Set consisting of widths of all sold connections within the microstructure

Table A1. Definitions of all physical quantities used in optimization formulation.

References

Brunet, T., Merlin, A., Mascaro, B., Zimny, K., Leng, J., Poncelet, O., Aristégui, C., Mondain-Monval, O., 2015. Soft 3D acoustic metamaterial with negative index. *Nat. Mater.* **14**, 384.

Christensen, J., & de Abajo, F.J.G., 2012. Anisotropic metamaterials for full control of acoustic waves. *Phys. Rev. Lett.* **108**, 124301.

Cheng, Y., Zhou, C., Yuan, B.G., Wu, D.J., Wei, Q., Liu, X.J., 2015. Ultra-sparse metasurface for high reflection of low-frequency sound based on artificial Mie resonances. *Nat. Mater.* **14**, 1013.

Christiansen, R.E., Wang, F., Sigmund, O., 2019. Topological insulators by topology optimization. *Phys. Rev. Lett.* **122**, 234502.

Chen, Y., Hu, G., Huang, G., 2017. A hybrid elastic metamaterial with negative mass density and tunable bending stiffness. *J. Mech. Phys. Solids* **105**, 179-198.

Chen, Y., Li, X., Nassar, H., Hu, G., Huang, G., 2018. A programmable metasurface for real time control of broadband elastic rays. *Smart. Mater. Struct.* **27**, 115011.

Dong, H.W., Zhao, S.D., Wang, Y.S., Zhang, C. 2017. Topology optimization of anisotropic broadband double-negative elastic metamaterials. *J. Mech. Phys. Solids* **105**, 54-80.

Dong, H.W., Zhao, S.D., Wang, Y.S., Zhang, C., 2018. Broadband single-phase hyperbolic elastic metamaterials for super-resolution imaging. *Sci. Rep.* **8**, 2247.

Dong, H.W., Zhao, S.D., Wei, P., Cheng, L., Wang, Y.S., Zhang, C., 2019. Systematic design and realization of double-negative acoustic metamaterials by topology optimization. *Acta Mater.* **172**, 102-120.

Fang, N., Xi, D., Xu, J., Ambati, M., Srituravanich, W., Sun, C., Zhang, X., 2006. Ultrasonic metamaterials with negative modulus. *Nat. Mater.* **5**, 452.

Fokin, V., Ambati, M., Sun, C., Zhang, X., 2007. Method for retrieving effective properties of locally resonant acoustic metamaterials. *Phys. Rev.* B **76**, 144302.

Goffaux, C., Vigneron, J.P., 2001. Theoretical study of a tunable phononic band gap system. *Phys. Rev.* B **64**, 075118.

Gerard, N.J., Li, Y., Jing, Y., 2018. Investigation of acoustic metasurfaces with constituent material properties considered. *J. Appl. Phys.* **123**, 124905.

Ward, G.P., Lovelock, R.K., Murray, A.R.J., Hibbins, A.P., Sambles, J.R., Smith, J.D., 2015. Boundary-layer effects on

acoustic transmission through narrow slit cavities, *Phys. Rev. Lett.* **115**, 044302.

Kaina, N., Lemoult, F., Fink, M., Lerosey, G., 2015. Negative refractive index and acoustic superlens from multiple scattering in single negative metamaterials. *Nature* **525**, 77.

Kadic, M., Milton, G.W., van Hecke, M., Wegener, M., 2019. 3D metamaterials. *Nature Reviews Physics* **1**.

Liu, Z., Zhang, X., Mao, Y., Zhu, Y.Y., Yang, Z., Chan, C.T., Sheng, P., 2000. Locally resonant sonic materials. *Science* **289**, 1734-1736.

Liang, Z., Li, J., 2012. Extreme acoustic metamaterial by coiling up space. *Phys. Rev. Lett.* **108**,114301.

Li, Y., Shen, C., Xie, Y., Li, J., Wang, W., Cummer, S.A., Jing, Y., 2017. Tunable asymmetric transmission via lossy acoustic metasurfaces. *Phys. Rev. Lett.* **119**, 035501.

Li, J., Shen, C., Díaz-Rubio, A., Tretyakov, S.A., Cummer, S.A., 2018. Systematic design and experimental demonstration of bianisotropic metasurfaces for scattering-free manipulation of acoustic wavefronts. *Nat. Commun.* **9**, 1342.

Li, X., Chen, Y., Hu, G., Huang, G., 2018. A self-adaptive metamaterial beam with digitally controlled resonators for subwavelength broadband flexural wave attenuation. *Smart. Mater. Struct.* **27**, 045015.

Lee, S.H., Park, C.M., Seo, Y.M., Wang, Z.G., Kim, C.K., 2010. Composite acoustic medium with simultaneously negative density and modulus. *Phys. Rev. Lett.* **104**, 054301.

Liu, Y., Su, X., Sun, C.T., 2015. Broadband elastic metamaterial with single negativity by mimicking lattice systems. *J. Mech. Phys. Solids* **74**, 158-174.

Liu, K., Zegard, T., Pratapa, P.P., Paulino, G.H., 2019. Unraveling tensegrity tessellations for metamaterials with tunable stiffness and bandgaps. *J. Mech. Phys. Solids* **131**, 147-166.

Ma, G. Sheng, P., 2016. Acoustic metamaterials: From local resonances to broad horizons. *Sci. Adv.* **2**, e1501595.

Ma, G., Fan, X., Sheng, P., Fink, M., 2018. Shaping reverberating sound fields with an actively tunable metasurface. *Proc. Natl. Acad. Sci.* **115**, 6638-6643.

Mei, J., Ma, G., Yang, M., Yang, Z., Wen, W., Sheng, P., 2012. Dark acoustic metamaterials as super absorbers for low-frequency sound. *Nat. Commun.* **3**, 756.

Morini, L., Eyzat, Y., Gei, M., 2019. Negative refraction in quasicrystalline multilayered metamaterials. *J. Mech. Phys. Solids* **124**, 282-298.

Nanthakumar, S.S., Zhuang, X., Park, H.S., Nguyena, C., Chen, Y., Rabczuk, T., 2019. Inverse design of quantum spin hall-based phononic topological insulators. *J. Mech. Phys. Solids* **125**, 550-571.

Pendry, J. B., 2000. Negative refraction makes a perfect lens. *Phys. Rev. Lett.* **85**, 3966.

Qi, S., Oudich, M., Li, Y., Assouar, B., 2016. Acoustic energy harvesting based on a planar acoustic metamaterial. *Appl. Phys. Lett.* **108**, 263501.

Song, B. H., Bolton, J. S., 2000. A transfer-matrix approach for estimating the characteristic impedance and wave numbers of limp and rigid porous materials. *J. Acoust. Soc. Am.* **107**, 1131-1152.

Shen, C., Xie, Y., Sui, N., Wang, W., Cummer, S.A., Jing, Y., 2015. Broadband acoustic hyperbolic metamaterial. *Phys. Rev. Lett.* **115**, 254301.

Sridhar, A., Liu, L., Kouznetsova, V.G., Geers, M.G.D., 2018. Homogenized enriched continuum analysis of acoustic metamaterials with negative stiffness and double negative effects. *J. Mech. Phys. Solids* **119**, 104-117.

Sugino, C., Ruzzene, M., Erturk, A., 2018. Merging mechanical and electromechanical bandgaps in locally resonant metamaterials and metastructures. *J. Mech. Phys. Solids* **116**, 323-333.

Xie, Y., Popa, B. I., Zigoneanu, L., Cummer, S.A., 2013. Measurement of a broadband negative index with space-coiling acoustic metamaterials. *Phys. Rev. Lett.* **110**, 175501.

Xie, Y., Wang, W., Chen, H., Konneker, A., Popa, B.I., Cummer, S.A., 2014. Wavefront modulation and subwavelength diffractive acoustics with an acoustic metasurface. *Nat. Commun.* **5**, 5553.

Xie, B., Tang, K., Cheng, H., Liu, Z., Chen, S., Tian, J., 2017. Coding acoustic metasurfaces. *Adv. Mater.* **29**, 1603507.

Xia, B., Wang, G., Zheng, S., 2019. Robust edge states of planar phononic crystals beyond high-symmetry points of Brillouin zones. *J. Mech. Phys. Solids* **124**, 471-488.

Yang, M., Ma, G., Yang, Z., Sheng, P., 2013. Coupled membranes with doubly negative mass density and bulk modulus. *Phys. Rev. Lett.* **110**, 134301.

Zhu, R., Liu, X.N., Hu, G.K., Sun, C.T., Huang, G.L., 2014. Negative refraction of elastic waves at the deep-subwavelength scale in a single-phase metamaterial. *Nat. Commun.* **5**, 5510.

Zhu, Y., Fan, X., Liang, B., Cheng, J., Jing, Y., 2017. Ultrathin acoustic metasurface-based Schroeder diffuser. *Phys. Rev. X* **7**, 021034.

Zhang, S., Yin, L., Fang, N., 2009. Focusing ultrasound with an acoustic metamaterial network. *Phys. Rev. Lett.* **102**, 194301.

Zhu, J., Christensen, J., Jung, J., Martin-Moreno, L., Yin, X., Fok, L., Zhang, X., Garcia-Vidal, F.J., 2011. A holey-structured metamaterial for acoustic deep-subwavelength imaging. *Nat. Phys.* **7**, 52-55.

Zigoneanu, L., Popa, B.I., Cummer, S.A., 2014. Three-dimensional broadband omnidirectional acoustic ground cloak. *Nat. Mater.* **13**, 352.

Zhou, Y., Fang, X., Li, D., Hao, T., Li, Y., 2018. Acoustic multiband double negativity from coupled single-negative resonators. *Phys. Rev. Appl.* **10**, 044006.